Analysis and Design of a T/S Compensated IPT System for AGV Maintaining Stable Output Current Versus Air Gap and Load Variations

Bin Yang, *Student Member, IEEE*, Yuanfang Lu, *Student Member, IEEE*, Yuner Peng, *Student Member, IEEE*, Shuangjiang He, Yang Chen, *Member, IEEE*, Zhengyou He, *Senior Member, IEEE*, Ruikun Mai, *Senior Member, IEEE*, and Zhulin Wang

***Abstract*—Inductive power transfer (IPT) technology for automatic guided vehicles wireless charging has widely drawn attention. The displacement of the air gap is inevitable due to tire pressure and spring deformation when vehicles are loaded with various weights. It can degrade the performance of the IPT system because the loosely coupled transformer parameters (self-inductances and mutual inductance) deviate from the designed values due to the position deviation of both sides' ferrite cores. In this article, a parameter design method based on T-series (T/S) topology is proposed to maintain stable output current versus air gap and load variation. Then, the parameter design process of the T/S topology to improve air gap misalignment performance is elaborated. Finally, a 20 A/1 kW experimental setup was built to verify the validity. Experimental results show that the output current fluctuation is within 4.71% when the load varies from 1.2 to 2.4 Ω and the air gap decreases from 90 to 30 mm (primary self-inductance, secondary self-inductance, and mutual inductance increase by 4.71%, 30.22%, and 121.52%, respectively). Moreover, the overall output current fluctuation is less than 6% when the secondary side moves along the track with the air gap varying from 30 to 90 mm.**

***Index Terms*—Air gap displacement, inductive power transfer (IPT), loosely coupled transformer (LCT) parameters, parameters design, stable output current.**

I. Introduction

INDUCTIVE power transfer (IPT) technique can transfer energy from power sources to loads without any physical contact. Compared with the traditional plug-in system, the IPT system is superior in security, convenience, etc. Therefore, it is widely employed in many applications such as consumer electronics [1], biomedical implant devices [2], underwater power supplies [3], electric vehicles [4], automatic guided vehicles (AGVs) [5], and so on.

Aiming to reduce the size of the battery pack and extend the working time of the vehicle, the dynamic IPT system is used for AGV charging [6], [7]. AGVs have high precision tracking capability [8], but the displacement of the air gap is inevitable due to tire pressure and spring deformation when the vehicles are loaded with different weights. In order to enable the IPT system to operate against air gap variations, many works of literature are investigated, and they can be roughly classified into two categories: control scheme and compensation topology design.

Some control schemes like phase-shift control [9] and variable frequency control [10] can realize the abovementioned targets. As an alternative method, a dc–dc converter can be employed on the primary or the secondary side to regulate the system output [11], [12]. However, RF communication is required in these approaches for the primary-side control technology. Moreover, an extensive range of modulation depth is usually desired against a large coupling variation, which may lead to the decrease of system efficiency and increase in the cost/complexity of IPT systems [13].

To simplify control schemes, the compensation topology design method, including hybrid topology and topology parameter optimization, is extensively studied because some topologies have the inherent characteristic of misalignment tolerance. For example, hybrid topologies are proposed by Zhao *et al.* [14], [15], Chen *et al.* [16], [17], and Qu *et al.* [18], taking advantage of two compensation topologies with opposite output characteristics over misalignment to maintain the total output relatively stable. However, the cost and complexity of the hybrid topologies are high due to a large number of passive components and coils. Besides, optimization of compensation parameters can also achieve relatively stable power transmission. A series–parallel–series topology is proposed by J. L. Villa to enhance the IPT system stability of transmission power against coupling variations [19]. In [20] and [21], two design methods of parameters are proposed by Feng *et al.* for series–series (S/S) and inductor–capacitor–capacitor–series topologies, respectively, to

Manuscript received August 7, 2021; revised October 29, 2021; accepted December 1, 2021. Date of publication December 14, 2021; date of current version January 19, 2022. This work was supported in part by the China Postdoctoral Science Foundation under Grant 2020M683352, in part by the National Natural Science Foundation of China under Grant 51977184, in part by the Special Fund from the Central Government to Guide the Development of Local Science and Technology in Shenzhen under Grant 2021Szvup122, and in part by the Sichuan S&T Innovation Project under Grant 2021116. Recommended for publication by Associate Editor A. Safaee. *(Corresponding author: Yang Chen.)*

Bin Yang, Yuanfang Lu, Yuner Peng, Yang Chen, Zhengyou He, and Ruikun Mai are with the School of Electrical Engineering, Southwest Jiaotong University, Chengdu 611756, China (e-mail: yb@my.swjtu.edu.cn; luyuanfang1997@163.com; pengyuner@my.swjtu.edu.cn; yangchen@swjtu.edu.cn; hezy@home.swjtu.edu.cn; mairk@swjtu.edu.cn).

Shuangjiang He is with Tangshan Institute, Southwest Jiaotong University, Tangshan 063000, China (e-mail: hsjhsj@my.swjtu.edu.cn).

Zhulin Wang is with Technology Industry Group, Southwest Jiaotong University, Chengdu 610031, China (e-mail: wang@swjtu.edu.cn).

Color versions of one or more figures in this article are available at https://doi.org/10.1109/TPEL.2021.3135053.

Digital Object Identifier 10.1109/TPEL.2021.3135053

obtain a small range fluctuation of transfer power against misalignments. However, loads of these approaches have to be fixed. To solve this weakness, Yao *et al.* [22], [23] utilize S/S-parallel and series–capacitor–inductor–capacitor topology with particle swarm optimization to achieve stable output voltage versus coupling coefficient and load variations. For the parameter optimization, it is only suitable for the case that the self-inductances of the loosely coupled transformer (LCT) are hardly changed with the coupling variation. Once the self-inductances of coils are changed with displacement, the misalignment performance of the IPT system is degraded.

As we know, ferrite cores are commonly used in the IPT system for the AGV to increase mutual inductance and decrease the effect of leaked electromagnetic field [24]. However, the use of ferrite cores can make LCT parameters (self-inductances and mutual inductance) more sensitive to the air gap [25]. When the air gap between the primary side and the secondary side is changed, the variations of LCT parameters cannot be neglected, which may destroy the resonant tank, even lead to instability and reduction in power transmission. Moreover, the battery charging voltage u_B of AGV is usually low (24–48 V), and the charging current i_B is typically high (more than 10 A), which means the battery equivalent load $R = u_B/ i_B$ is a resistance of several Ohms. Therefore, the IPT system for the AGV wireless charging has to provide a constant output current for the battery, while the air gap and load are both changeable during the operation process.

In this article, to overcome the above-mentioned issues, a T-series (T/S) topology is used for the AGV wireless charging. There are three components on the primary side and one on the secondary side, which can reduce the installation space of the vehicle and offer sufficient design freedom for the IPT system. Then, a novel parameter design method considering the LCT parameters variations is proposed to obtain stable output current versus air gap and load variations for AGV charging by optimizing the parameter values of the T/S topology. For the LCT parameters variations, both self-inductance and mutual inductance are taken into consideration, which is not studied in the prior works.

The rest of this article is organized as follows. In Section II, the analysis of the T/S topology for maintaining a stable output current is described. The parameter design procedure and an example are introduced in Section III. In Section IV, a 1-kW prototype is built to verify the theoretical analysis. Finally, Section V concludes this article.

II. Theoretical Analysis

As shown in Fig. 1(a), a typical schematic diagram of AGV dynamic charging is given. With the utilization of the ferrite cores, the magnetic flux density increases when the secondary side approaches the primary side because the ferrite core of the secondary side serves as a small reluctance, increasing the self-inductances and mutual inductance of the LCT [24]. Therefore, the profile of the LCT parameters for the IPT system with ferrite cores and coupled coils on the primary and secondary sides can be depicted in Fig. 1(b). A long track LCT structure

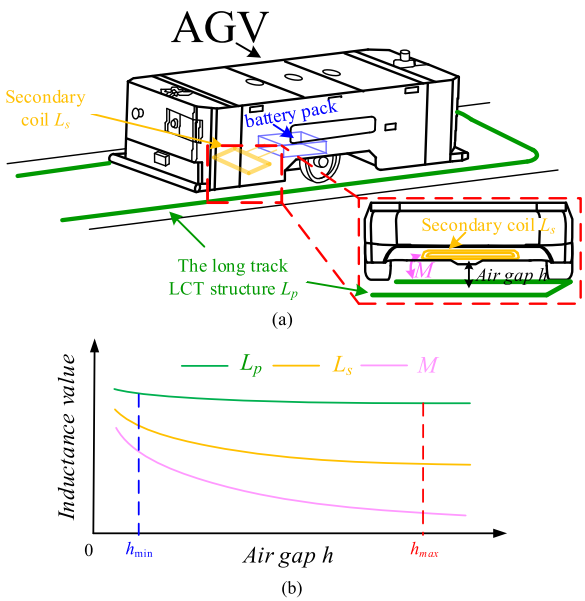

Fig. 1. Typical schematic diagram of AGV dynamic charging. (a) Charging process of AGV. (b) Corresponding variation trend of LCT parameters with different h, where L_p and L_s are the self-inductances of the LCT on the primary and secondary sides, respectively. M is the mutual inductance of the LCT. $h_{\min}$ and $h_{\max}$ mean the minimum and maximum of the predetermined range of air gap h, respectively.

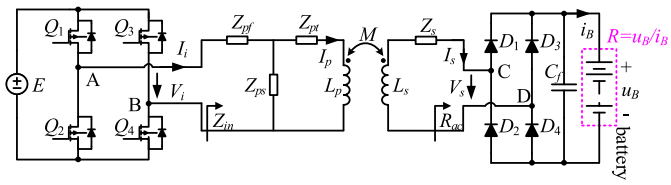

Fig. 2. T/S compensated topology.

is used in this article. And LCT parameters L_s, L_p, and M are expressed as (1). [$h_{\min}$–$h_{\max}$] is the predetermined range of air gap h, the corresponding variation range of the LCT parameters are defined as [$L_{p\min}$–$L_{p\max}$], [$L_{s\min}$–$L_{s\max}$], and [$M_{\min}$–$M_{\max}$], respectively. It is noticed that the variation of the mutual inductance is more prominent in practice. Since the values of M, L_p, and L_s decrease with the rise of air gap h, the derivates of LCT parameters should satisfy $d(M(h))/dh<0$, $d(L_p(h))/dh <0$, and $d(L_s(h))/dh<0$

$$\begin{cases} L_p = L_p(h) \\ L_s = L_s(h) \\ M = M(h). \end{cases} \tag{1}$$

As shown in Fig. 2, a T/S compensated topology is given. Z_{pf}, Z_{ps}, Z_{pt}, and Z_s are the impedances of each component, as illustrated in (2). X_{pf}, X_{ps}, X_{pt}, and X_s are the reactance of each component, which are inductors if the values are positive; otherwise, they are capacitors. The duty cycle of the inverter is set as 50%, and the angular frequency of the system is $\omega = 2\pi f$, where f represents the switching frequency of the inverter. E, u_B, and i_B are the input dc voltage, output dc voltage, and output dc current, respectively. They can be expressed by (3), respectively

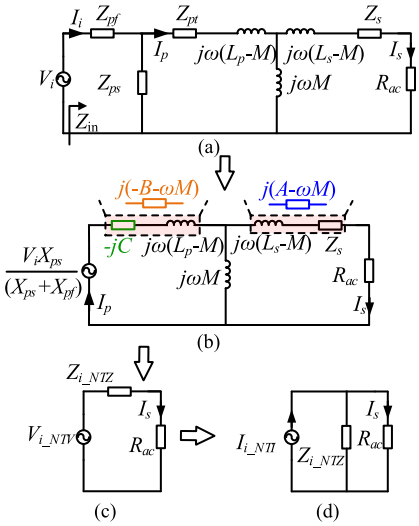

Fig. 3. Equivalent circuit of T/S compensated topology. (a) is the T-type equivalent model. (b)–(d) are the Norton and Thevenin's equivalent models, where $A = \omega L_s + X_s$, $B = C - \omega L_p$, $C = X_{ps}^2/(X_{ps}+X_{pf}) - X_{ps} - X_{pt}$.

[26]

$$Z_{pf} = jX_{pf}, Z_{ps} = jX_{ps}, Z_{pt} = jX_{pt}, Z_s = jX_s \quad (2)$$

$$E = \frac{\pi}{2\sqrt{2}}\dot{V}_i, u_B = \frac{\pi}{2\sqrt{2}}\dot{V}_s, i_B = \frac{2\sqrt{2}}{\pi}\dot{I}_s. \quad (3)$$

$R_{\rm ac}$ is the equivalent ac load. The relationship between $R_{\rm ac}$ and the battery equivalent load R can be given by [27]

$$R_{\rm ac} = \frac{8}{\pi^2}R. \quad (4)$$

A. Maintaining Stable Output Current Versus Load Variation

To simplify the analysis, the resistance of each reactive element is neglected. The fundamental harmonic approximation method is used to calculate the output current of the system. According to Norton and Thevenin's theorem, the T/S topology circuit shown in Fig. 3(a) can be simplified as Fig. 3(b)–(d). In Fig. 3(b), we have $-jC + j\omega(L_p - M) = j(-\omega M)$ and $Z_s + j\omega(L_s - M) = j(A - \omega M)$.

In Fig. 3(c) and (d), V_{i_NTV}, Z_{i_NTZ}, and I_{i_NTI} are expressed as

$$\begin{cases} V_{i\_NTV} = -\frac{V_i X_{ps}\omega M}{(X_{ps}+X_{pf})B} \\ Z_{i\_NTZ} = j\left(A + \omega^2 M^2/B\right) \\ I_{i\_NTI} = \frac{V_{i\_NTV}}{Z_{i\_NTZ}}. \end{cases} \quad (5)$$

According to Fig. 3(c) and (d), if the ratio of $|Z_{i\_NTV}|$ to $|R_{\rm ac}|$ is larger, the fluctuation of the current I_s is smaller. Hence, a variable α is used to represent the sensitivity of the output current over $R_{\rm ac}$ as shown in the following:

$$\alpha = \frac{|Z_{i\_NTZ}|^2}{{R_{\rm ac}}^2} = \frac{\left(A + \omega^2 M^2/B\right)^2}{{R_{\rm ac}}^2}. \quad (6)$$

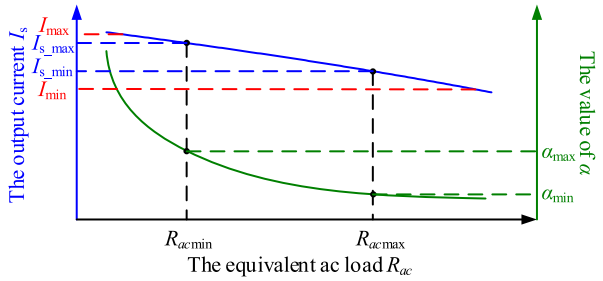

Fig. 4. Profile of output current I_s and α with $R_{\rm ac}$ variation, where α is the defined variable to represent the sensitivity of the output current over $R_{\rm ac}$, and I_s is the ac output current of the IPT system. $R_{\rm ac}$ is the equivalent ac load, of which the variation range is $[R_{\rm acmin}, R_{\rm acmax}]$, and the corresponding α and I_s are $[\alpha_{\min}, \alpha_{\max}]$ and $[I_{s\_\min}, I_{s\_\max}]$, respectively. $I_{\min}$ and $I_{\max}$ are the minimum and maximum allowable currents, respectively.

Furthermore, the ac output current I_s can be obtained as

$$I_s = \frac{V_{i\_NTV}}{Z_{i\_NTZ} + R_{\rm ac}}. \quad (7)$$

From (6) and (7), the profile of the ac output current I_s and α can be given as Fig. 4 when $B \neq 0$. It can be seen that the ac output current I_s and α decrease with $R_{\rm ac}$. Within the load variation range $[R_{\min}$–$R_{\max}]$ (the corresponding variation range of $R_{\rm ac}$ is $[R_{ac\min}$–$R_{ac\max}]$), the maximum output current I_s and α are $I_{s\_\max}$ and $\alpha_{\max}$ when $R_{\rm ac} = R_{\rm acmin}$, while the minimum values are $I_{s\_\min}$ and $\alpha_{\min}$ when $R_{\rm ac} = R_{\rm acmax}$. The allowable current range of the system can be defined as $[I_{\min}$–$I_{\max}]$, and a variable β is defined to describe the allowable fluctuation of the output current, as

$$\frac{I_{\max} - I_{\min}}{I_{\max} + I_{\min}} = \beta. \quad (8)$$

If the fluctuation of output current is lower than the required fluctuation β when $R_{\rm ac}$ varies from $R_{\rm acmin}$ to $R_{\rm acmax}$, i.e., (9), the output current is regarded as a constant value, namely, we can obtain stable output current I_s versus the load variation when $\alpha \geq \alpha_{\min}$

$$\frac{I_{s\_\max} - I_{s\_\min}}{I_{s\_\max} + I_{s\_\min}} \leq \beta. \quad (9)$$

Due to the monotony of I_s as shown in Fig. 4, the maximum allowable range of load variation can be obtained when the fluctuation of output current is equal to the allowable fluctuation β, namely, $I_{s\_\max} = I_{\max}$ and $I_{s\_\min} = I_{\min}$.

B. Maintaining Stable Output Current Versus LCT Parameters Variations

According to (7), Fig. 3(c) and (d), to maintain stable output current within the predefined range $[h_{\min}$–$h_{\max}]$, the absolute value of the ac equivalent source V_{i_NTV} and the equivalent impedance Z_{i_NTZ} should have the same variation trend versus h.

Combining (1) and (5), the derivate of the ac equivalent source $|V_{i\_NTV}|$ and the equivalent impedance $|Z_{i\_NTZ}|$ with respect to h can be given as (10) shown at the bottom of the next page. From (10), there are three cases as Fig. 5 for the variation trend of the ac equivalent source V_{i_NTV} as follows:

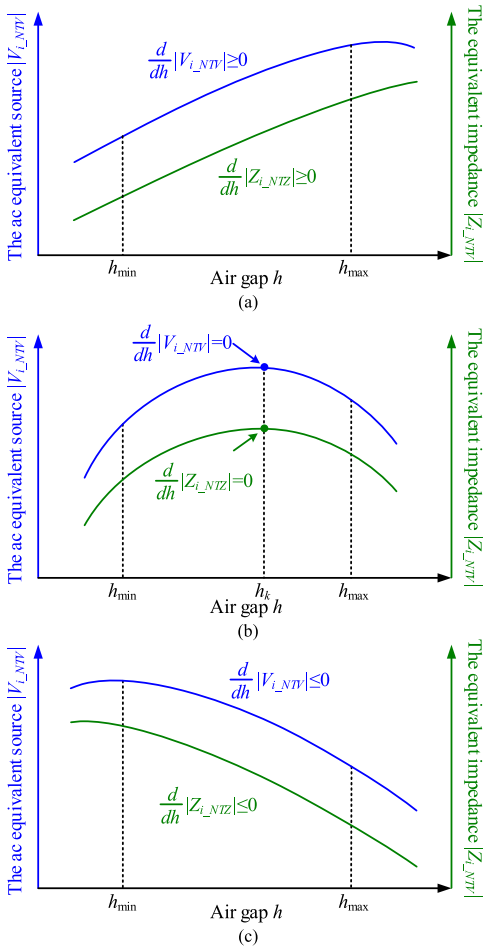

Fig. 5. Profile of the ac equivalent source $|V_{i\_NTV}|$ and the equivalent impedance $|Z_{i\_NTZ}|$ versus air gap h for (a) Case I, (b) Case II, and (c) Case III.

Case I: The absolute value of the ac equivalent source $|V_{i\_NTV}|$ increases with h, namely

$$\frac{d}{dh}\left(|V_{i\_NTV}|\right)\geq 0. \tag{11}$$

To maintain the same trend with $|V_{i\_NTV}|$, we have

$$\frac{d}{dh}\left(|Z_{i\_NTZ}|\right)\geq 0. \tag{12}$$

Substituting (11) and (12) into (10), the value range of C and X_s can be calculated in (A1) of the Appendix.

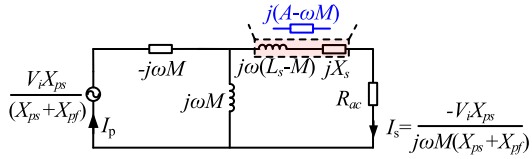

Fig. 6. Circuit and output current for *case I* if the self-inductance is constant or slightly variable.

In practice, the self-inductance L_p and L_s will approach a constant value with the increase of h in loosely coupling IPT system, resulting in $dL_p(h)/dh$ and $dL_s(h)/dh$ approaching zero. Then, L_p and L_s can be regarded as two constant values, C will be approximatively equal to ωL_p according to (10) and (A1) in the Appendix, and the corresponding circuit and output current can be described in Fig. 6. From Fig. 6, the output current I_s is inversely proportional to M, which means the system has the inferior misalignment tolerance versus air gap variation.

Case II: The absolute value of the ac equivalent source $|V_{i\_NTV}|$ is nonmonotonic with h. From (10), if there is a value of air gap h_k within the predetermined air gap $[h_{\min}$–$h_{\max}]$ to satisfy (13), $|Z_{i\_NTZ}|$ and $|V_{i\_NTV}|$ will simultaneously reach extreme at h_k to ensure the same variation trend

$$\begin{cases}\frac{d}{dh}\left(|V_{i\_NTV}|\right)=0\\ \frac{d}{dh}\left(|Z_{i\_NTZ}|\right)=0\end{cases},h=h_k\in(h_{\min},h_{\max}). \tag{13}$$

Substituting (13) into (10), C can be calculated as

$$\begin{cases}C=\omega L_p(h_k)-\omega M(h_k)\frac{dL_p(h_k)/dh}{dM(h_k)/dh}\\ =\omega L_p(h_k)-\omega M(h_k)\frac{dM(h_k)/dh}{dL_s(h_k)/dh}\end{cases},h_k\in(h_{\min},h_{\max}). \tag{14}$$

From (14), we have

$$\frac{dL_p(h_k)/dh}{dM(h_k)/dh}=\frac{dM(h_k)/dh}{dL_s(h_k)/dh},h_k\in(h_{\min},h_{\max}). \tag{15}$$

According to (15), the ratios between the derivative of $L_p(h)$, $M(h)$, and $L_s(h)$ are required to be the same, while it is hard to be achieved unless the LCT is specially designed, which is almost impossible in practice.

Case III: The absolute value of the ac equivalent source $|V_{i\_NTV}|$ decreases with h. Similarly, we have

$$\begin{cases}\frac{d}{dh}\left(|V_{i\_NTV}|\right)\leq 0\\ \frac{d}{dh}\left(|Z_{i\_NTZ}|\right)\leq 0.\end{cases} \tag{16}$$

Substituting (16) into (10), the value range of C and X_s can be calculated as (A2) in the Appendix.

$$h\in(h_{\min},h_{\max})$$

$$\begin{cases}\frac{d}{dh}\left(|V_{i\_NTF}|\right)=\left|\frac{V_iX_{p1}}{(X_{p1}+X_{pf})}\right|\frac{d}{dh}\left(\left|\frac{\omega M(h)}{B(h)}\right|\right)=\begin{cases}\left|\frac{V_iX_{p1}}{(X_{p1}+X_{pf})}\right|+\frac{\omega B(h)\frac{dM(h)}{dh}+\omega^2M(h)\frac{dL_p(h)}{dh}}{B(h)^2},B(h)>0\\ \left|\frac{V_iX_{p1}}{(X_{p1}+X_{pf})}\right|\frac{-\omega B(h)\frac{dM(h)}{dh}-\omega^2M(h)\frac{dL_p(h)}{dh}}{B(h)^2},B(h)\leq 0\end{cases}\\ \frac{d}{dh}\left(|Z_{i\_NTZ}|\right)=\frac{d}{dh}\left(\left|A(h)+\frac{\omega^2M(h)^2}{B(h)}\right|\right)=\begin{cases}\omega\frac{dL_2(h)}{dh}+\frac{2\omega^2B(h)M(h)\frac{dM(h)}{dh}+\omega^3M(h)^2\frac{dL_p(h)}{dh}}{B(h)^2},A(h)+\frac{\omega^2M^2}{B(h)}>0\\ \omega\frac{dL_2(h)}{dh}-\frac{2\omega^2B(h)M(h)\frac{dM(h)}{dh}+\omega^3M(h)^2\frac{dL_p(h)}{dh}}{B(h)^2},A(h)+\frac{\omega^2M^2}{B(h)}\leq 0\end{cases}\end{cases} \tag{10}$$

where

$$A(h)=\omega L_s(h)+X_s,B(h)=C-\omega L_p(h)$$

From (A2), the high design flexibility can be obtained in this case. Moreover, it can be applied in any range of air gap variations, and the design of LCT is not rigorous. Thus, compared to *Case I* and *Case II*, *Case III* is more practical.

Due to the high design freedom and the wide value range of C and X_s, this article utilizes *case III* to discuss the implementation of the IPT system with a stable output current. The variation range of the battery equivalent load is defined as [$R_{\min}$–$R_{\max}$], the corresponding variation range of $R_{\rm ac}$ is [$R_{\rm acmin}$–$R_{\rm acmax}$]). α will decrease with the increase of air gap h or the battery equivalent load R in terms of (6), which will reach the minimum value $\alpha_{\min}$ when $R_{\rm ac} = R_{\rm acmax}$, $h = h_{\max}$ ($L_p = L_{p\min}$, $L_s = L_{s\min}$, and $M = M_{\min}$), namely, the fluctuation of the output current will increase with the air gap h when $R_{\rm ac}$ varies from $R_{\rm acmax}$ to $R_{\rm acmin}$. $\alpha_{\min}$ can be written as

$$\alpha_{\min} = \frac{\left(A_{\min} + \omega^2 {M_{\min}}^2 / B_{\max}\right)^2}{{R_{ac\max}}^2} \tag{17}$$

where

$$A_{\min} = \omega L_{s\min} + X_s, B_{\max} = C - \omega L_{p\min}.$$

C. Constraints of Maintaining Stable Output Current Versus LCT Parameters and Load Variations

Combining (3), (4), (5), and (7), the current gain can be obtained as

$$G = \left|\frac{I_s}{V_i}\right| = \sqrt{\frac{\omega^2 M^2 {X_{ps}}^2/(X_{ps}+X_{pf})^2}{(AB+\omega^2 M^2)^2 + {R_{\rm ac}}^2 B^2}}. \tag{18}$$

The allowable current gain range of the system is defined as [$G_{\min}$–$G_{\max}$]. We can set the current gain to be $G_{\min}$ when $R_{\rm ac} = R_{\rm acmax}$ and $h = h_{\min}$ ($L_p = L_{p\max}$, $L_s = L_{s\max}$, and $M = M_{\max}$), the current gain $G_{\min}$ can be given as (19), which can be employed as the first constraint

$$G_{\min} = \sqrt{\frac{\omega^2 {M_{\max}}^2 {X_{ps}}^2/(X_{ps}+X_{pf})^2}{\left(A_{\max}B_{\min} + \omega^2 {M_{\max}}^2\right)^2 + {R_{\rm ac\max}}^2 {B_{\min}}^2}} \tag{19}$$

where

$$A_{\max} = \omega L_{s\max} + X_s$$

$$B_{\min} = {X_{ps}}^2/(X_{ps}+X_{pf}) - (X_{ps}+X_{pt}+\omega L_{p\max}).$$

In order to make the current gain located between $G_{\min}$ and $G_{\max}$ with a large air gap variation, there are two cases for the maximum current gain $G_{G\max}$ when the load changes from $R_{\rm acmax}$ to $R_{\rm acmin}$.

Case a: The current gain can reach the maximum value $G_{G\max}$ when $R_{\rm ac} = R_{\rm acmin}$ and $h = h_{\max}$ ($L_p = L_{p\min}$, $L_s = L_{s\min}$, and $M = M_{\min}$).

Case b: The maximum current gain $G_{G\max}$ is the extreme point when $R_{\rm ac} = R_{\rm acmin}$.

According to the variation trend of α, the profile of G can be roughly depicted in Fig. 7(a) and (b) for *Case a* and *Case b*, respectively. Then, the allowable gain fluctuation β can be

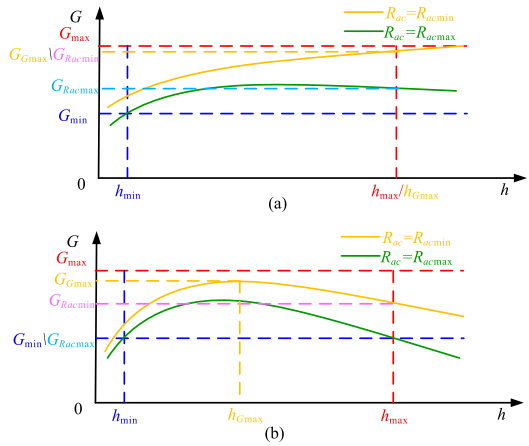

Fig. 7. Profile of G considering the LCT parameters and load variations. (a) is *case a*, and (b) is *case b*. $G_{G\max}$ is the maximum current gain and the corresponding air gap is $h_{G\max}$. G_{Racmin} and G_{Racmax} are the current gains when $h = h_{\max}$ ($L_p = L_{p\min}$, $L_s = L_{s\min}$, and $M = M_{\min}$), $R_{\rm ac} = R_{\rm acmin}$ or $R_{\rm ac} = R_{\rm acmax}$, respectively.

expressed as

$$\beta = \frac{G_{\max} - G_{\min}}{G_{\max} + G_{\min}}. \tag{20}$$

When $R_{\rm ac} = R_{\rm acmin}$ or $R_{\rm ac} = R_{\rm acmax}$, $h = h_{\max}$ ($L_p = L_{p\min}$, $L_s = L_{s\min}$, and $M = M_{\min}$), the current gains G_{Racmin} and G_{Racmax} can be given as

$$\begin{cases} G_{Rac\min} = \sqrt{\dfrac{\omega^2 {M_{\min}}^2 {X_{ps}}^2/(X_{ps}+X_{pf})^2}{\left(A_{\min}B_{\max}+\omega^2 {M_{\min}}^2\right)^2 + {R_{ac\min}}^2 {B_{\max}}^2}} \\ G_{Rac\max} = \sqrt{\dfrac{\omega^2 {M_{\min}}^2 {X_{ps}}^2/(X_{ps}+X_{pf})^2}{\left(A_{\min}B_{\max}+\omega^2 {M_{\min}}^2\right)^2 + {R_{ac\max}}^2 {B_{\max}}^2}}. \end{cases} \tag{21}$$

According to (9) and (20), we can obtain the second constraint of the system, i.e.,

$$\frac{G_{Rac\min} - G_{Rac\max}}{G_{Rac\min} + G_{Rac\max}} \le \beta. \tag{22}$$

Substituting (21) into (22), the second constraint of the system can be written as

$$\frac{\sqrt{\dfrac{1}{1+{R_{ac\min}}^2/{R_{ac\max}}^2\alpha_{\min}}} - \sqrt{\dfrac{1}{1+1/\alpha_{\min}}}}{\sqrt{\dfrac{1}{1+{R_{ac\min}}^2/{R_{ac\max}}^2\alpha_{\min}}} + \sqrt{\dfrac{1}{1+1/\alpha_{\min}}}} \le \beta. \tag{23}$$

In Fig. 7(a), $G_{G\max}$ and G_{Racmin}, $h_{\max}$ and $h_{G\max}$ satisfy

$$\begin{cases} G_{G\max} = G_{Rac\min} = \sqrt{\dfrac{\omega^2 {M_{\min}}^2 {X_{ps}}^2/(X_{ps}+X_{pf})^2}{\left(A_{\min}B_{\max}+\omega^2 {M_{\min}}^2\right)^2 + {R_{ac\min}}^2 {B_{\max}}^2}} \\ h_{\max} = h_{G\max}. \end{cases} \tag{24}$$

In order to achieve the maximum load variations, $G_{G\max}$ (G_{Racmin}) should be equal to $G_{\max}$, as shown in (25), which can be employed as the third constraint of the system for *Case a*

$$G_{G\max} = G_{Rac\min} = G_{\max}$$

$$= \sqrt{\frac{\omega^2 {M_{\min}}^2 {X_{ps}}^2/(X_{ps}+X_{pf})^2}{\left(A_{\min}B_{\max} + \omega^2 {M_{\min}}^2\right)^2 + {R_{ac\min}}^2 {B_{\max}}^2}}. \tag{25}$$

In Fig. 7(b), when load $R_{\rm ac} = R_{\rm acmin}$, the current gain $G_{Rac} = {}_{Racmin}$ can be described as

$$G_{R_{\rm ac}=R_{\rm acmin}} = \sqrt{\frac{\omega^2 M^2 {X_{ps}}^2/(X_{ps}+X_{pf})^2}{(AB+\omega^2M^2)^2+{R_{\rm ac\,min}}^2B^2}}. \quad (26)$$

Substituting (1) into (26), and making the derivative of (26) equal to zero, the $h_{G\max}$ can be solved, as follows:

$$\frac{d\left(G_{R_{\rm ac}=R_{\rm acmin}}(h)\right)}{dh}$$

$$= \frac{d}{dh}\left(\sqrt{\frac{\omega^2 M(h)^2 {X_{ps}}^2/(X_{ps}+X_{pf})^2}{\left(A(h)B(h)+\omega^2M(h)^2\right)^2+{R_{\rm ac\,min}}^2B(h)^2}}\right)$$

$$= 0 \overset{\text{solve}h}{\rightarrow} h_{G\max}. \quad (27)$$

Substituting the calculation result of (27) into (26), $G_{G\max}$ can be obtained. To achieve the maximum load variations, $G_{G\max}$ should be equal to $G_{\max}$, which is the third constraint of the system for *Case b*, as given in (28)

$$G_{G\max} = G_{\max} \quad (28)$$

$$Z_{\rm in} = \frac{V_i}{I_i} = \frac{B(R_{\rm ac}+jA)(X_{ps}+X_{pf})+j\omega^2M^2(X_{ps}+X_{pf})}{(R_{\rm ac}+jA)\left(j{X_{ps}}^2/(X_{ps}+X_{pf})-jB\right)+\omega^2M^2}$$

$$\tan\theta = \left(\frac{1}{(X_{ps}+X_{pf})} - \frac{{X_{ps}}^2}{B(X_{ps}+X_{pf})^2}\right)\frac{1}{R_{\rm ac}G^2} + \sqrt{\alpha}. \quad (29)$$

Based on Kirchhoff's Law, the input impedance $Z_{\rm in}$ can be solved. And the input impedance angle θ can be expressed as (29). Generally, zero-voltage switching (ZVS) is preferred because it can decrease the switching loss of the inverter. To achieve the ZVS condition, the turn-OFF current is required to be adequate to discharge the junction capacitor of the switching devices [13]. Hence, the value of tanθ should always be positive during the whole dynamic charging process, which can be used as the fourth constraint, as follows:

$$\tan\theta > 0. \quad (30)$$

III. Parameters Design and Example

A. LCT Multivariate Fitting Method

According to the above analysis, we can only roughly acquire the constraints of the system. It seems complicated and hard to precisely design the parameters of each reactive element because the LCT self-inductances are also variable during the whole charging process. If the number of the variables can be reduced, the parametric design of the IPT system will be simplified.

The long track is one of the typical LCT structures in AGV wireless charging, as depicted in Fig. 8(a). ANSYS MAXWELL is used to assist the design. The air gap is defined as h. With different air gaps h, corresponding LCT parameters are displayed in Fig. 8(b). MATLAB can be employed to fit these

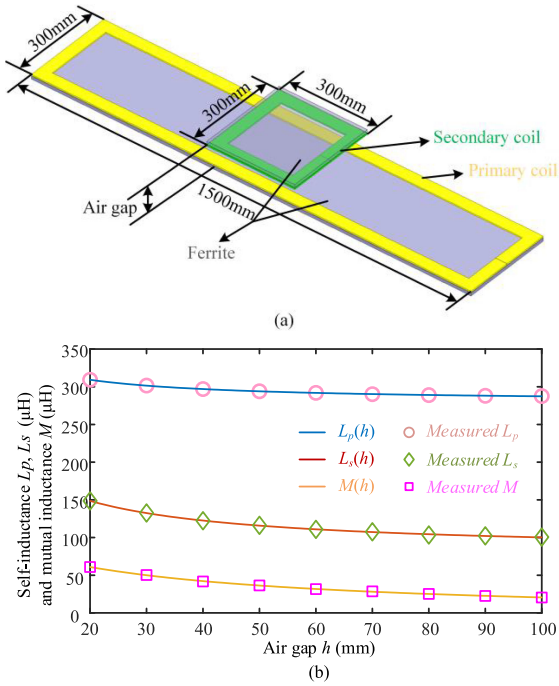

Fig. 8. (a) Simplified LCT and (b) corresponding LCT parameters with different air gaps when the secondary side is located in the middle of the primary side.

discrete points of LCT parameters [16]. Then, the variations of the LCT parameters can be expressed by some function related to the same variable, e.g., (31). The fitting results are drawn in Fig. 8(b) to compare with the measured LCT parameters, which demonstrates that the fitted function is almost consistent with the measured data over different air gaps h

$$\begin{cases} L_p = L_p(h) = \frac{279.7h+3062}{h+7.987} \\ L_s = L_s(h) = \frac{80.89h+3124}{h+11.9} \\ M = M(h) = \frac{-4.788h+3156}{h+30.2}. \end{cases} \quad (31)$$

It is noted that LCT parameters can also be written as functions with the other same variable, i.e., coupling coefficient, primary/secondary self-inductance or mutual inductance, and four fitting forms are given in (32). Moreover, the fitted formula types are various, such as division of polynomial, polynomial, exponential, and so on, as shown in (33). The differences mainly lie in the complexity of calculation for different types of fitting

$$\begin{cases} L_s = L_s(k) \\ L_p = L_p(k) \\ M = M(k) \end{cases} \begin{cases} L_s = L_s(L_s) \\ L_p = L_p(L_s) \\ M = M(L_s) \end{cases} \begin{cases} L_s = L_s(L_p) \\ L_p = L_p(L_p) \\ M = M(L_p) \end{cases}$$

$$\begin{cases} L_s = L_s(M) \\ L_p = L_p(M) \\ M = M(M) \end{cases} \quad (32)$$

$$\begin{cases} f(X) = \frac{p_0+p_1X+p_2X^2+\cdots+p_nX^n}{q_0+q_1X+q_2X^2+\cdots+q_mX^m} \\ f(X) = p_0+p_1X+p_2X^2+\cdots+p_nX^n \\ f(X) = k_0e^{p_0+p_1X+p_2X^2+\cdots+p_nX^n} \\ \quad\vdots \end{cases} \quad (33)$$

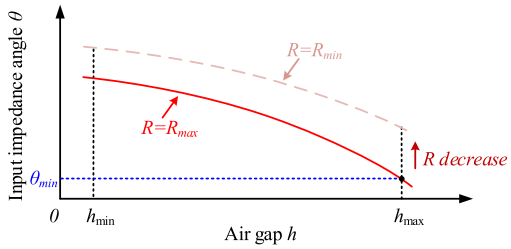

Fig. 9. Variation trend of θ.

B. Parameters Design Procedure

For the fourth constraint, an iterative algorithm can be used to satisfy (30) within [$h_{\min}$–$h_{\max}$] and [$R_{\min}$–$R_{\max}$]. Theoretically, any value of LCT parameters and load can be considered as a reference value, the corresponding impedance angle function can be used to assist the design of X_{ps}, X_{pt}, X_{pf}, and X_s. For example, when $R = R_{\max}$, $h = h_{\max}$ ($L_p = L_{p\min}$, $L_s = L_{s\min}$, and $M = M_{\min}$), the corresponding impedance angle $\theta_{\min}$ can be given as

$$\theta_{\min} = \arctan\left[\left(\frac{1}{(X_{ps}+X_{pf})} - \frac{{X_{ps}}^2}{B_{\max}(X_{ps}+X_{pf})^2}\right)\frac{(8/\pi^2)}{{R_{ac\max}}^2 G_{Rac\max}^2} + \sqrt{\alpha_{\min}}\right]. \quad (34)$$

This article focuses on the analysis and design of a T/S topology for AGV dynamic IPT system maintaining stable output current with the long track LCT structure. Hence, the fluctuation of L_p is relatively small (only 4.71%) compared with L_s (30.22%) and M (121.52%) according to Fig. 8. Then, L_p and G can be approximatively considered as two constant values to simplify the fourth constraint. From (29), it can be found that the variation trend of tanθ is consistent with α, which means input impedance angle θ can reach the minimum value $\theta_{\min}$ during the whole operating region when the battery equivalent load and air gap are $R_{\max}$ and $h_{\max}$ ($L_p = L_{p\min}$, $L_s = L_{s\min}$, and $M = M_{\min}$). Furthermore, the fourth constraint can be simplified as tan$\theta_{\min} \geq 0$. And the corresponding variation trend of θ can be depicted in Fig. 9.

For other applications, the variation trend of θ may be hard to evaluate due to the relatively large fluctuation of L_p. Hence, we can use an iterative algorithm to satisfy (30). A common design method is given as follows.

First, the values of $G_{\min}$, β, $R_{\min}$, $R_{\max}$, $\theta_{\min}$, the size of LCT, and the variation range of air gap [$h_{\min}$–$h_{\max}$] are given. Referring to (32) and (33), LCT parameters over air gap h variation can be fitted into functions with the same variable. Then, substituting the values of β, $R_{\min}$, and $R_{\max}$ into (23), the boundary conditions of $\alpha_{\min}$ can be determined. Next, by choosing an appropriate $\alpha_{\min}$ and substituting the value of $\alpha_{\min}$, $G_{\min}$, β, $R_{\min}$, $R_{\max}$, $\theta_{\min}$, and the fitted functions into (6), (19), (34), (25), or (28), the value of X_{pf}, X_{ps}, X_{pt}, and X_s can be solved. An iterative algorithm to obtain optimal parameters satisfying (30) within [$h_{\min}$–$h_{\max}$] and [$R_{\min}$–$R_{\max}$]. Finally, the results should be checked by (A2) of Appendix, when the results can not satisify (A2) of the Appendix, the $\alpha_{\min}$ will be amended to recalculate the results based on the boundary condition. The flow chart is depicted in Fig. 10 to further explain the design procedure.

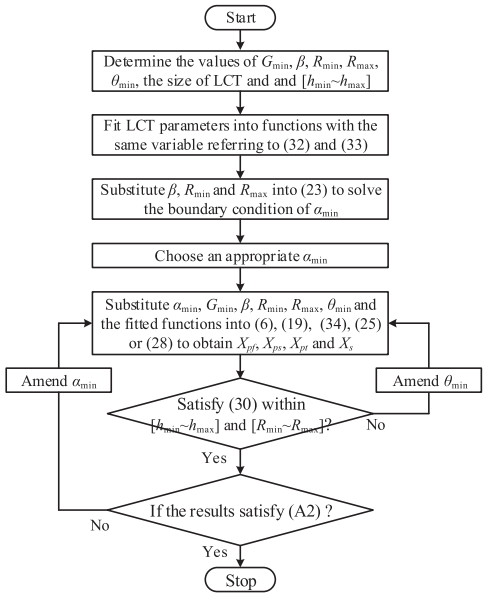

Fig. 10. Design flowchart of the system parameters.

TABLE I
PARAMETER VALUES

Parameter	Value			
$\alpha_{\min}$	10	5	3.67	3.13
X_{pf}	-12.4 Ω	-17.38 Ω	-21.17 Ω	-24.06 Ω
X_{ps}	9.83 Ω	11.45 Ω	12.51 Ω	13.27 Ω
X_{pt}	-148.93 Ω	-149.69 Ω	-150.66 Ω	-151.48 Ω
X_s	-45.55 Ω	-46.32 Ω	-46.52 Ω	-46.57 Ω

C. Example of the Design for AGV

An IPT system is designed for AGV charging employing the design method presented above. The operating frequency f is 85 kHz. The dc output current i_B and dc input voltage E are 20 A and 200 V, the input impedance angle $\theta_{\min}$ is 0°, the fluctuation of the output current β is 5%, the variation range of the battery load R is designed as 1.2–2.4 Ω because the voltage range of the AGV is regarded as 24–48 V. The air gap h is 30–90 mm, and the size of LCT is shown in Fig. 8. From (23), the boundary conditions of $\alpha_{\min}$ can be calculated as 3.13.

Based on the boundary of $\alpha_{\min}$ and the design steps in Fig. 10, the parameters can be calculated accordingly. Theoretically, larger $\alpha_{\min}$ can lead to better performance of the system maintaining stable output current versus load variation. However, it may affect the overall performance of the IPT system. In order to explore the effects of $\alpha_{\min}$, the four sets of parameters are calculated in Table I with different $\alpha_{\min}$. Based on Kirchhoff's law and the parameters in Table I, the current of each circuit loop, the input impedance angle θ and α can be calculated, and the corresponding curves are given in Fig. 11.

From Fig. 11, it can be seen that the variation trend of α and θ are consistent with the theoretical analysis, and the fluctuation of output current I_s can satisfy the design requirements, which

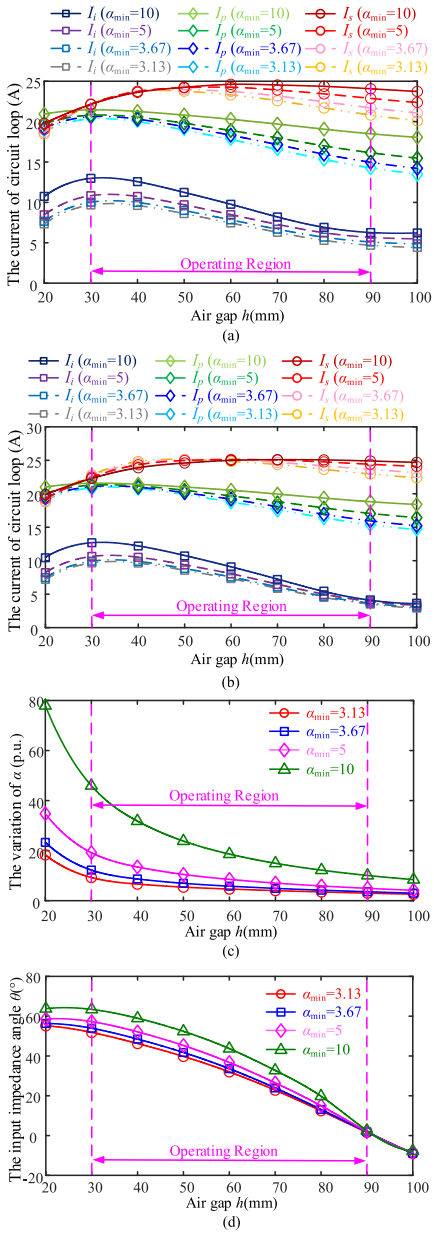

Fig. 11. Current in each circuit loop, the value of α, and the input impedance angle versus h when (a) $R = 2.4\ \Omega$, (b) $R = 1.2\ \Omega$, (c) $R = 2.4\ \Omega$, and (d) $R = 2.4\ \Omega$.

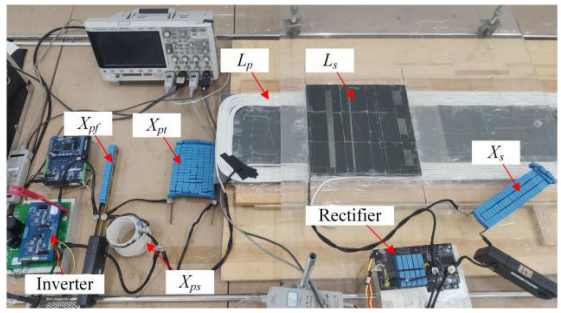

Fig. 12. Schematic diagram of the experimental porotype.

TABLE II
MEASURED PARAMETER VALUES

Parameter	Design value	Parameter	Design value
E	200V	i_B	20A
f	85kHz	*Air gap h*	30~90mm
M	50.13~22.63μH	k	0.28~0.13
L_p	301.59~288.03μH	L_s	133.51~102.53μH
X_{pf}	-19.84 Ω	X_{ps}	12.53 Ω
X_{pt}	-149.70 Ω	X_s	-47.08 Ω
r_{Xpf}	0.015 Ω	r_{Xps}	0.011 Ω
r_{Xpt}	0.012 Ω	r_{Xs}	0.01 Ω
r_{Lp}	0.27 Ω	r_{Ls}	0.075 Ω

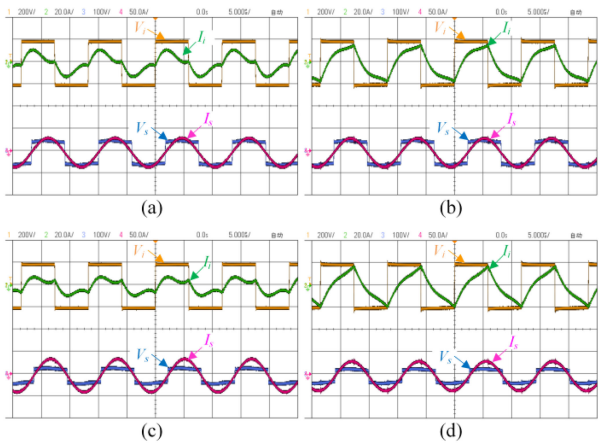

Fig. 13. Experimental waveforms. (a) $R = 2.4\ \Omega$ and air gap = 90 mm. (b) $R = 2.4\ \Omega$ and air gap = 30 mm. (c) $R = 1.2\ \Omega$ and air gap = 90 mm. (d) $R = 1.2\ \Omega$ and air gap = 30 mm.

can show the feasibility of the proposed method. Besides, when $\alpha_{\min}$ increases, the output current is more stable in the operating region over air gap and load variation, but the current of each circuit loop will also increase, resulting in a reduction of the efficiency. As a compromise, $\alpha_{\min}$ is selected to be the minimum that satisfies the fluctuation requirement (5%) of the output current within the predefined operation region [$h_{\min}$–$h_{\max}$] of the air gap h.

IV. Experimental Results

To demonstrate the applicability of the proposed method, a 1-kW experimental prototype was built, as shown in Fig. 12. The optimal $\alpha_{\min}$ is 3.67, which can be obtained by a simple iterative algorithm according to the design flowchart, as shown in Fig. 10. System parameters are listed in Table II, r_{Xpf}, r_{Xpt}, r_{Xps}, r_{Xs}, r_{Lp}, and r_{Ls} are internal resistance of each reactive element, respectively. An electronic load (IT8816B) is used to verify the performance of the IPT system. The MOSFETs Q_1–Q_4 are C2M0040120D and the rectifier diodes D_1–D_4 are DSSK 60-015A.

A. Experimental Results at a Fixed Position

In this part, the secondary side stops at a fixed position while the air gap and load are changed. The experimental results are presented as follows. Fig. 13(a) and (b) shows the experimental waveforms of the output current/voltage of the inverter and input current/voltage of the rectifier at $R = 2.4\ \Omega$ with different air gaps. Fig. 13(c) and (d) shows the experimental waveforms at $R = 1.2\ \Omega$ with different air gaps. The variation trend of input

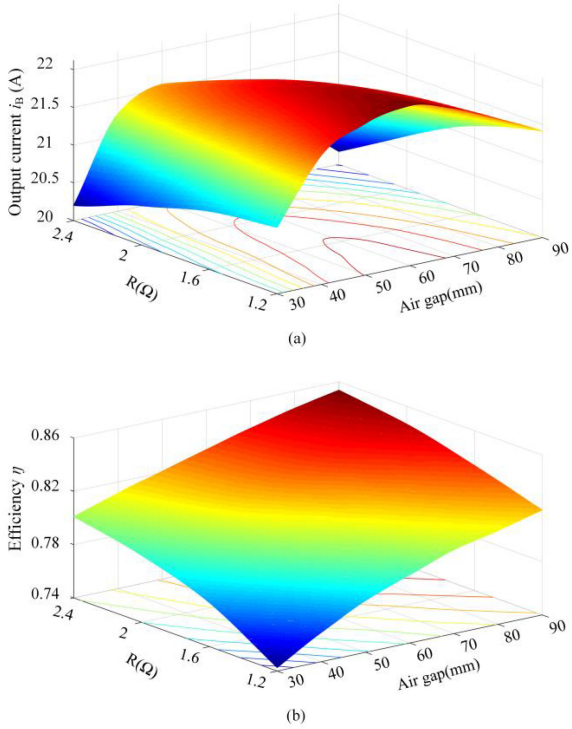

Fig. 14. Measured experimental results versus R and air gap variation. (a) is the output current and (b) is the efficiency.

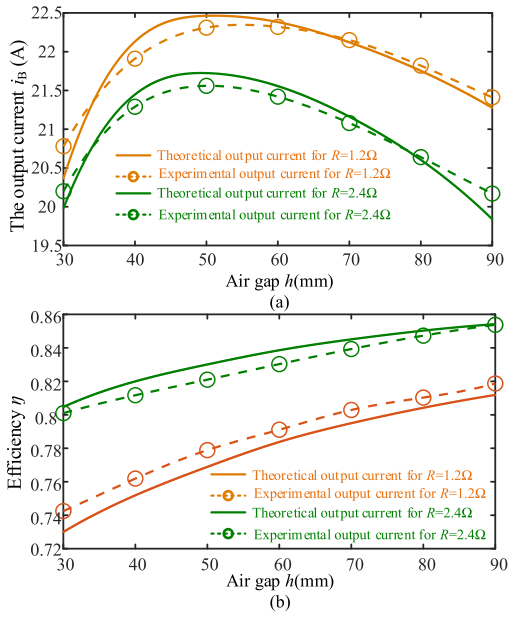

Fig. 15. Comparison of the theoretical and experimental for (a) output current and (b) efficiency.

impedance angle is consistent with the theoretical analysis. And the soft turn-ON for semiconductor switches can be verified.

The output current is measured and depicted in Fig. 14(a), which illustrates the output current of the designed system versus air gap and load variation. With air gap variation (30–90 mm), the fluctuation of the output current is less than 4.71%, while the load is changed from 1.2 to 2.4 Ω. The results demonstrate that the system has good performance of stable current output.

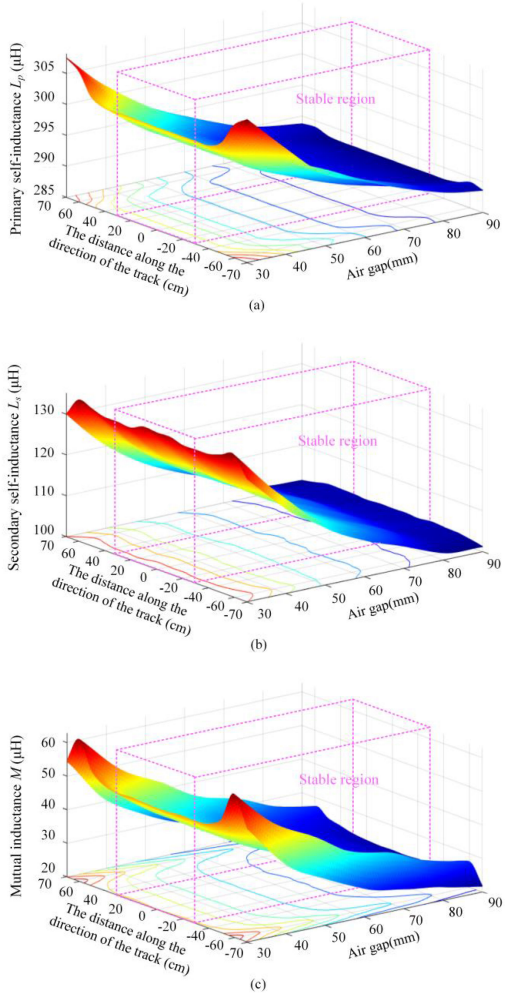

Fig. 16. LCT parameters during the dynamic charging process. (a) is the primary self-inductance L_p, (b) is the secondary self-inductance L_s, and (c) is the mutual inductance M.

The corresponding efficiency is drawn in Fig. 14(b). It can be observed that the efficiency of the designed system gradually decays with the decrease of the air gap (85.38% drops to74.25%). When the air gap falls to 30 mm with $R = 1.2\ \Omega$, the efficiency reaches the lowest point (74.25%). The decline of efficiency is mainly attributed to a high current in each circuit loop on the primary side and a light load on the secondary side. Considering the low-voltage and high-current working conditions [5], the experimental results are acceptable.

Fig. 15 shows the theoretical prediction of the output current and the efficiency [27]. The maximu error of the output current is 0.82% (0.33 A) when $h = 90$ mm and $R = 2.4\ \Omega$ and the maximum error of the efficiency is 0.9% when $h = 30$ mm and $R = 1.2\ \Omega$. Meanwhile, the error is inevitable and it mainly comes from the deviation of the parameters and the resistance of each reactive element. The results demonstrate the availability of the theoretical analysis.

B. Experimental Results in the Dynamic Charging Process

In this part, a dynamic experiment is implemented, i.e., the secondary side moves along the track. The corresponding LCT

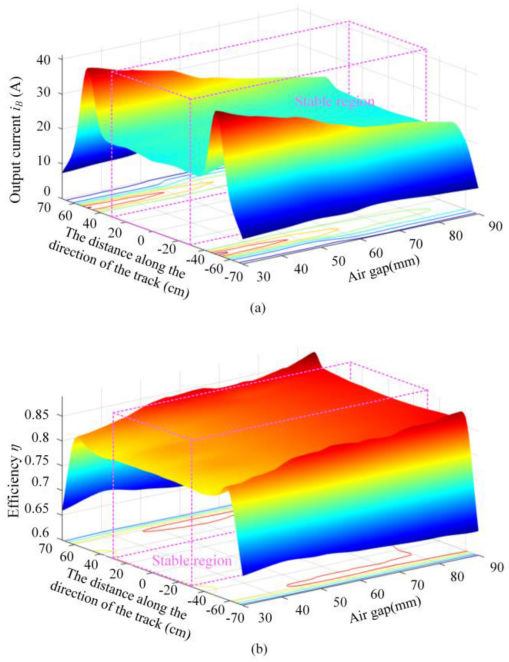

Fig. 17. Experimental results. (a) Output current during the dynamic charging process. (b) Corresponding efficiency.

parameters variations and the experimental results are, respectively, listed in Figs. 16 and 17, where $R = 2.4\ \Omega$. It can be seen that the stable region of the output current is [−30–30 cm] along the direction of the track. With a rise of 300% in the air gap from 30 to 90 mm in the operation region, the LCT parameters change dramatically, i.e., the variation ranges of L_p, L_s, and M are [301.59–288.03 μH], [133.51–102.53 μH], and [50.13–22.63 μH], respectively. From the experimental results, when the secondary side operates along the direction of the track, the output current does not significantly change (the fluctuation of the output current is [20.17–22.13 A]). The efficiency declines with the decrease of the air gap because the variation of the LCT parameters leads to a worse detuned situation causing a higher loop current, but it remains almost constant with the same air gap (the variation range of the efficiency is [79.64%–86.06%]). When the secondary side moves out of the stable region (approach to the edge of the track), the value of the LCT parameters will not be stable in the same air gap, resulting in the unstable output current. In this article, the maximum unstable output current is more than 40 A. Hence, the current/voltage stress of the component needs to be considered in practice. Besides, we also should avoid this case, such as using the external protection circuit or the preplaced roadblock in the track.

As a result, the designed system can obtain a relatively stable output current versus air gap and load variations during the dynamic charging process. And the results also show that the proposed method is suitable for the application of the LCT parameters changing with a variable air gap, such as AGV.

V. Conclusion

In summary, the transfer current gain is significantly affected by the LCT parameters when the IPT system has a large air gap variation. With the equivalent circuit and mathematical analysis of T/S topology, the key parameter affecting the output current versus load is identified. Besides, the cases of maintaining stable output current against air gap variation are discussed. Based on the constraints of the output current, the LCT multivariate fitting method is introduced to simplify the design. Moreover, a parameter design method is proposed to obtain the required fluctuation of the output current in the IPT system. In the experiment, the output current fluctuation is less than 4.71% when L_p, L_s, M, and R vary from 288.03 to 301.59 μH, 102.53 to 133.51 μH, 22.63 to 50.13 μH, and 1.2 to 2.4 Ω, respectively. When the secondary side moves along the track from −30 to 30 cm with the air gap changing from 30 to 90 mm, the output current varies from 20.17 to 22.13 A at $R = 2.4\ \Omega$. The results validate the good performance of the proposed method for the AGV wireless charging system versus air gap and load variations. Additionally, there are some limitations in the proposed approach, such as low efficiency, high unstable output current when the secondary side

$$h \in (h_{\min}, h_{\max})$$

$$\begin{cases} \min\left(\omega L_p\left(h\right)\right) \geq C \geq \max\left(\omega L_p\left(h\right) - \omega M\left(h\right)\frac{dL_p(h)/dh}{dM(h)/dh}\right) \\ C \leq \min\left(\frac{\omega\left(L_p(h)dL_s(h)/dh - M(h)\left(dM(h)/dh - \sqrt{(dM(h)/dh)^2 - (dL_p(h)/dh)(dL_s(h)/dh)}\right)\right)}{dL_s(h)/dh}\right) \\ C \geq \max\left(\frac{\omega\left(L_p(h)\frac{dL_s(h)}{dh} - M(h)\left(dM(h)/dh + \sqrt{(dM(h)/dh)^2 - (dL_p(h)/dh)(dL_s(h)/dh)}\right)\right)}{dL_s(h)/dh}\right) \\ X_s \geq \max\left(-\omega L_s\left(h\right) - \frac{\omega^2 M(h)^2}{C - \omega L_p(h)/dh}\right) \end{cases}$$

or

$$\begin{cases} \min\left(\omega L_p\left(h\right)\right) \geq C \geq \max\left(\omega L_p\left(h\right) - \omega M\left(h\right)\frac{dL_p(h)/dh}{dM(h)/dh}\right) \\ C \geq \max\left(\frac{\omega\left(L_p(h)dL_s(h)/dh - M(h)\left(dM(h)/dh + \sqrt{(dM(h)/dh)^2 - (dL_p(h)/dh)(dL_s(h)/dh)}\right)\right)}{dL_s(h)/dh}\right) \\ C \leq \min\left(\frac{\omega\left(L_p(h)\frac{dL_s(h)}{dh} - M(h)\left(dM(h)/dh - \sqrt{(dM(h)/dh)^2 - (dL_p(h)/dh)(dL_s(h)/dh)}\right)\right)}{dL_s(h)/dh}\right) \\ X_s \leq \min\left(-\omega L_s\left(h\right) - \frac{\omega^2 M(h)^2}{C - \omega L_p(h)/dh}\right) \end{cases} \tag{A1}$$

$$h \in (h_{\min}, h_{\max}) \begin{cases} C \geq \max\left(\omega L_p\left(h\right)\right) \\ X_s \geq \max\left(-\omega L_s\left(h\right) - \frac{\omega^2 M(h)^2}{C - \omega L_p(h)/dh}\right) \end{cases}$$

or

$$\begin{cases} C \leq \min\left(\omega L_p\left(h\right)\right), C \leq \min\left(\omega L_p\left(h\right) - \omega M\left(h\right) \frac{dL_p(h)/dh}{dM(h)/dh}\right) \\ X_s \geq \max\left(-\omega L_s\left(h\right) - \frac{\omega^2 M(h)^2}{C - \omega L_p(h)/dh}\right) \end{cases}$$

or

$$\begin{cases} C \geq \max\left(\frac{\omega\left(L_p(h) dL_s(h)/dh - M(h)\left(dM(h)/dh + \sqrt{(dM(h)/dh)^2 - (dL_p(h)/dh)(dL_s(h)/dh)}\right)\right)}{dL_s(h)/dh}\right) \\ C \leq \min\left(\frac{\omega\left(L_p(h)\frac{dL_s(h)}{dh} - M(h)\left(dM(h)/dh - \sqrt{(dM(h)/dh)^2 - (dL_p(h)/dh)(dL_s(h)/dh)}\right)\right)}{dL_s(h)/dh}\right) \\ C \leq \min\left(\omega L_p\left(h\right)\right), C \leq \min\left(\omega L_p\left(h\right) - \omega M\left(h\right) \frac{dL_p(h)/dh}{dM(h)/dh}\right) \\ X_s \leq \min\left(-\omega L_s\left(h\right) - \frac{\omega^2 M(h)^2}{C - \omega L_p(h)/dh}\right) \end{cases} \tag{A2}$$

moves out of the stable region (approach to the edge of the track), which will be improved in the future.

APPENDIX

(A1) shown at the bottom of the previous page, where $\min(*)$ and $\max(*)$ mean the minimum and maximum value of $*$. (A2) shown at the top of this page.

REFERENCES

[1] S. Y. Hui, "Planar wireless charging technology for portable electronic products and qi," *Proc. IEEE*, vol. 101, no. 6, pp. 1290–1301, Jun. 2013.

[2] A. K. RamRakhyani, S. Mirabbasi, and M. Chiao, "Design and optimization of resonance-based efficient wireless power delivery systems for biomedical implants," *IEEE Trans. Biomed. Eng.*, vol. 5, no. 1, pp. 48–63, Feb. 2011.

[3] H. Fukuda *et al.*, "New concept of an electromagnetic usage for contactless communication and power transmission in the ocean," in *Proc. IEEE Int. Underwater Technol. Symp.*, 2013, pp. 1–4.

[4] W. Y. Lee *et al.*, "Finite-width magnetic mirror models of mono and dual coils for wireless electric vehicles," *IEEE Trans. Power Electron.*, vol. 28, no. 3, pp. 1413–1428, Mar. 2013.

[5] F. Lu *et al.*, "A tightly-coupled inductive power transfer system for low-voltage and high-current charging of automatic guided vehicles," *IEEE Trans. Ind. Electron.*, vol. 66, no. 9, pp. 6867–6875, Sep. 2019.

[6] M. Budhia, J. T. Boys, G. A. Covic, and C. Huang, "Development of a single-sided flux magnetic coupler for electric vehicle IPT charging systems," *IEEE Trans. Ind. Electron.*, vol. 60, no. 1, pp. 318–328, Jan. 2013.

[7] A. Zaheer, G. A. Covic, and D. Kacprzak, "A bipolar pad in a 10-kHz 300-W distributed IPT system for AGV applications," *IEEE Trans. Ind. Electron.*, vol. 61, no. 7, pp. 3288–3301, Jul. 2014.

[8] S. Li, G. Zhang, X. Lei, X. Yu, H. Qian, and Y. Xu, "Trajectory tracking control of a unicycle-type mobile robot with a new planning algorithm," in *Proc. Int. Conf. Robot. Biomimetics*, 2017, pp. 780–786.

[9] A. Berger, M. Agostinelli, S. Vesti, J. A. Oliver, J. A. Cobos, and M. Huemer, "A wireless charging system applying phase-shift and amplitude control to maximize efficiency and extractable power," *IEEE Trans. Power Electron.*, vol. 30, no. 11, pp. 6338–6348, Nov. 2015.

[10] H. Hu, T. Cai, S. Duan, X. Zhang, J. Niu, and H. Feng, "An optimal variable frequency phase shift control strategy for ZVS operation within wide power range in IPT systems," *IEEE Trans. Power Electron.*, vol. 35, no. 5, pp. 5517–5530, May 2020.

[11] J. M. Miller, O. C. Onar, and M. Chinthavali, "Primary-side power flow control of wireless power transfer for electric vehicle charging," *IEEE J. Emerg. Sel. Topics Power Electron.*, vol. 3, no. 1, pp. 147–162, Mar. 2015.

[12] Z. Yan *et al.*, "Efficiency improvement of wireless power transfer based on multitransmitter system," *IEEE Trans. Power Electron.*, vol. 35, no. 9, pp. 9011–9023, Sep. 2020.

[13] Y. Chen *et al.*, "Reconfigurable topology for IPT system maintaining stable transmission power over large coupling variation," *IEEE Trans. Power Electron.*, vol. 35, no. 5, pp. 4915–4924, May 2020.

[14] L. Zhao, D. J. Thrimawithana, and U. K. Madawala, "Hybrid bidirectional wireless EV charging system tolerant to pad misalignment," *IEEE Trans. Ind. Electron.*, vol. 64, no. 9, pp. 7079–7086, Sep. 2017.

[15] L. Zhao, D. J. Thrimawithana, U. K. Madawala, A. P. Hu, and C. C. Mi, "A misalignment-tolerant series-hybrid wireless EV charging system with integrated magnetics," *IEEE Trans. Power Electron.*, vol. 34, no. 2, pp. 1276–1285, Feb. 2019.

[16] Y. Chen, B. Yang, Z. Kou, Z. He, G. Cao, and R. Mai, "Hybrid and reconfigurable IPT systems with high-misalignment tolerance for constant-current and constant-voltage battery charging," *IEEE Trans. Power Electron.*, vol. 33, no. 10, pp. 8259–8269, Oct. 2018.

[17] Y. Chen *et al.*, "A hybrid inductive power transfer system with misalignment tolerance using quadruple-D quadrature pads," *IEEE Trans. Power Electron.*, vol. 35, no. 6, pp. 6039–6049, Jun. 2020.

[18] X. Qu, Y. Yao, D. Wang, S. Wong, and C. K. Tse, "A family of hybrid IPT topologies with near load-independent output and high tolerance to pad misalignment," *IEEE Trans. Power Electron.*, vol. 35, no. 7, pp. 6867–6877, Jul. 2020.

[19] J. L. Villa, J. Sallan, J. F. Sanz Osorio, and A. Llombart, "High-misalignment tolerant compensation topology for ICPT systems," *IEEE Trans. Ind. Electron.*, vol. 59, no. 2, pp. 945–951, Feb. 2012.

[20] H. Feng, T. Cai, S. Duan, X. Zhang, H. Hu, and J. Niu, "A dual-side detuned series-series compensated resonant converter for wide charging region in a wireless power transfer system," *IEEE Trans. Ind. Electron.*, vol. 65, no. 3, pp. 2177–2188, Mar. 2018.

[21] H. Feng, T. Cai, S. Duan, J. Zhao, X. Zhang, and C. Chen, "An LCC-compensated resonant converter optimized for robust reaction to large coupling variation in dynamic wireless power transfer," *IEEE Trans. Ind. Electron.*, vol. 63, no. 10, pp. 6591–6601, Oct. 2016.

[22] Y. Yao, Y. Wang, X. Liu, Y. Pei, D. Xu, and X. Liu, "Particle swarm optimization-based parameter design method for S/CLC-compensated IPT systems featuring high tolerance to misalignment and load variation," *IEEE Trans. Power Electron.*, vol. 34, no. 6, pp. 5268–5282, Jun. 2019.

[23] Y. Yao, Y. Wang, X. Liu, Y. Pei, and D. Xu, "A novel unsymmetrical coupling structure based on concentrated magnetic flux for high-misalignment IPT applications," *IEEE Trans. Power Electron.*, vol. 34, no. 4, pp. 3110–3123, Apr. 2019.

[24] S. Y. Jeong, J. H. Park, G. P. Hong, and C. T. Rim, "Autotuning control system by variation of self-inductance for dynamic wireless EV charging with small air gap," *IEEE Trans. Power Electron.*, vol. 34, no. 6, pp. 5165–5174, Jun. 2019.

[25] J. S. Choi, S. Y. Jeong, B. G. Choi, S. -T. Ryu, C. T. Rim, and Y.-S. Kim, "Air-gap-insensitive IPT pad with ferromagnetic and conductive plates," *IEEE Trans. Power Electron.*, vol. 35, no. 8, pp. 7863–7872, Aug. 2020.

[26] R. W. Erickson and D. Maksimovic, *Fundamentals of Power Electronics, Part IV Modern Rectifiers and Power System Harmonics, at Chapter 17 Line-Commutated Rectifier*, 2nd ed. Norwell, MA, USA: Kluwer, 2001, pp. 609–632.

[27] Y. Chen *et al.*, "Variable-parameter T-circuit-based IPT system charging battery with constant current or constant voltage output," *IEEE Trans. Power Electron.*, vol. 35, no. 2, pp. 1672–1684, Feb. 2020.

Bin Yang (Student Member, IEEE) received the B.S. degree in electrical engineering and automation from the School of Electrical and Automation Engineering, East China Jiaotong University, Nanchang, China, in 2017. He is currently working toward the Ph.D. degree with the School of Electrical Engineering, Southwest Jiaotong University, Chengdu, China.

His research interests include wireless power transfer, especially on misalignment tolerance improvement.

Yuanfang Lu (Student Member, IEEE) received the B.S. degree in electrical engineering and automation in 2019 from the School of Electrical Engineering, Southwest Jiaotong University, Chengdu, China, where he is currently working toward the B.Sc. degree with the School of Electrical Engineering.

His research interests include wireless power transfer.

Yuner Peng (Student Member, IEEE) received the B.S. degree in electrical engineering and automation in 2020 from the School of Electrical Engineering, Southwest Jiaotong University, Chengdu, China, where she is currently working toward the Ph.D. degree with the School of Electrical Engineering.

Her research interests include misalignment tolerance improvement of wireless power transfer and high-frequency wireless power transfer.

Shuangjiang He received the B.S. degree in electrical engineering and automation from the School of Electrical Engineering, Changsha University of Science and Technology, Changsha, China, in 2019. He is currently working toward the B.Sc. degree with the School of Tangshan Graduate, Southwest Jiaotong University, Tangshan, China.

His research interests include wireless power transfer.

Yang Chen (Member, IEEE) received the B.Sc. degree in electrical engineering and automation and the Ph.D. degree in electrical engineering from Southwest Jiaotong University, Chengdu, China, in 2015 and 2020, respectively.

From December 2018 to December 2019, he was a joint Ph.D. student founded by the China Scholarship Council with the Future Energy Electronics Center, Virginia Tech, Blacksburg, VA, USA. He is currently a Postdoctoral Researcher with Southwest Jiaotong University, Chengdu, China. His research interests include wireless power transfer.

Zhengyou He (Senior Member, IEEE) received the B.Sc. and M. Sc. degrees in computational mechanics from Chongqing University, Chongqing, China, in 1992 and 1995, respectively, and the Ph.D. degree from the School of Electrical Engineering, Southwest Jiaotong University, Chengdu, China, in 2001.

He is currently a Professor with the School of Electrical Engineering, Southwest Jiaotong University. His research interests include signal process and information theory applied to electrical power system, and application of wavelet transforms in power system.

Ruikun Mai (Senior Member, IEEE) received the B.Sc. and Ph.D. degrees in electrical engineering from the School of Electrical Engineering, Southwest Jiaotong University, Chengdu, China, in 2004 and 2010, respectively.

He is currently a Professor with the School of Electrical Engineering, Southwest Jiaotong University, Chengdu, China. His research interests include wireless power transfer and its application in railway systems, power system stability and control.

Zhulin Wang received the B.Sc. degree in economics and the M.Sc. degree in project management engineering from Southwest Jiaotong University, Chengdu, China, in 2001 and 2010, respectively.

He is currently an Engineer with Technology Industry Group, Southwest Jiaotong University. He has served as a Director of the Operation Department of the Information Network Center, Southwest Jiaotong University, the Director of the Development Department of Science and Technology Industry Group, and the Executive Director of the Institute of Modern Management, Southwest Jiaotong University. His research interests include system integration, software architecture, rail transit intelligent operation and maintenance, and wireless power transfer and its application.